Observations of near-bed orbital velocities and small-scale bedforms on the Dutch lower shoreface

Jebbe J. van der Werf [a,b,*], Reinier A. Schrijvershof [a,c], Laura B. Brakenhoff [d], Bart T. Grasmeijer [a]

[a] Department of Marine & Coastal Systems, Deltares, P.O. Box 177, 2600 MH Delft, The Netherlands
[b] Department of Water Engineering & Management, University of Twente, P.O. Box 217, 7500 AE Enschede, The Netherlands
[c] Department of Environmental Sciences, Wageningen University & Research, P.O. Box 9101, 6700 HB Wageningen, The Netherlands
[d] Department of Physical Geography, Faculty of Geosciences, Utrecht University, Princetonlaan 8a, 3584 CB Utrecht, The Netherlands

ARTICLE INFO

ABSTRACT

The lower shoreface, with water depths between about 8 and 20 m, forms the transition between the inner shelf and upper shoreface. Knowledge of the lower shoreface is essential, as it is – in many cases – the sediment source for the upper shoreface and beach. This paper presents new data of near-bed orbital velocities and small-scale bedforms at various depths and locations on the Dutch lower shoreface. Near-bed orbital velocities were beyond 1 m/s during high-energetic wave conditions. They increase with wave height and decrease with water depth, and can be reasonably well described by linear wave theory. Ripple heights range between 0.01 − 0.03 m and ripple lengths between 0.08 − 0.20 m. Ripple dimensions are controlled by wave mobility, with lower and shorter ripples for higher waves, and not so much by the currents. The Van Rijn (2007) formula generally overpredicts the ripple heights, and the variation with tidal currents in time. The measurements clearly indicate significant sediment mobility at the lower shoreface under higher wave events. It is yet unclear what this means for the net sand transport. This will depend on the subtle timing of sediment suspension, wave-mean currents and near-bed orbital velocities. It requires detailed modeling to determine lower shoreface net transport rates, and to unravel the controlling sand transport mechanisms.

1. Introduction

The lower shoreface, with water depths between about 8 and 20 m, forms the transition between the inner shelf and upper shoreface. Lower shoreface sand transport is controlled by the combined action of waves and currents (Van Rijn, 1997). It is covered by multiple types of bedforms ranging from small-scale ripples (a few decimeters long), tidal sand waves (100–1000 m long) to shoreface-connected ridges (5–10 km long) (Passchier and Kleinhans, 2005).

Knowledge of lower shoreface sand transport and seabed morphodynamics is essential, as the lower shoreface controls to a large degree how offshore seabed activities and climate change affect nearshore functions such as coastal safety. This concerns the effect of sea level rise on coastal evolution, as well as the impact of offshore wind farms, sand extraction and other human interferences. The lower shoreface is, in many cases, the sediment source for the upper shoreface and beach, and also mediates onshore wave energy transfer (Anthony and Aagaard, 2020).

However, the lower shoreface sand transport processes are complex and poorly understood. Sand transport across the lower shoreface is controlled by various competing, non-linear processes due to waves (e.g. wave skewness), currents (e.g. tidal currents and density-gradient driven currents in case of river outflow) and wave–current interactions (e.g. the Longuet-Higgins (1953) wave bottom boundary streaming). The relative importance of these sand transport mechanisms depends on many variables, such as wind and wave conditions, river discharge, water depth and bed composition. Lower shoreface sand transport is highly episodic with little sand movement during frequent fair-weather conditions, and large transport rates during rare storms.

Understanding lower shoreface sand transport is further complicated by the dynamic interaction with bedforms, occurring over a wide range of scales. Small-scale ripples (a few decimeters long and a few centimeters in height) are of particular interest. These ripples generate form roughness and affect near-bed turbulence, which influences sand transport. Storms can wash out these small-scale bedforms such that upper plane-bed, sheet-flow sand transport occurs with high transport rates confined to a few centimeters thick near-bed layer (Passchier and Kleinhans, 2005).
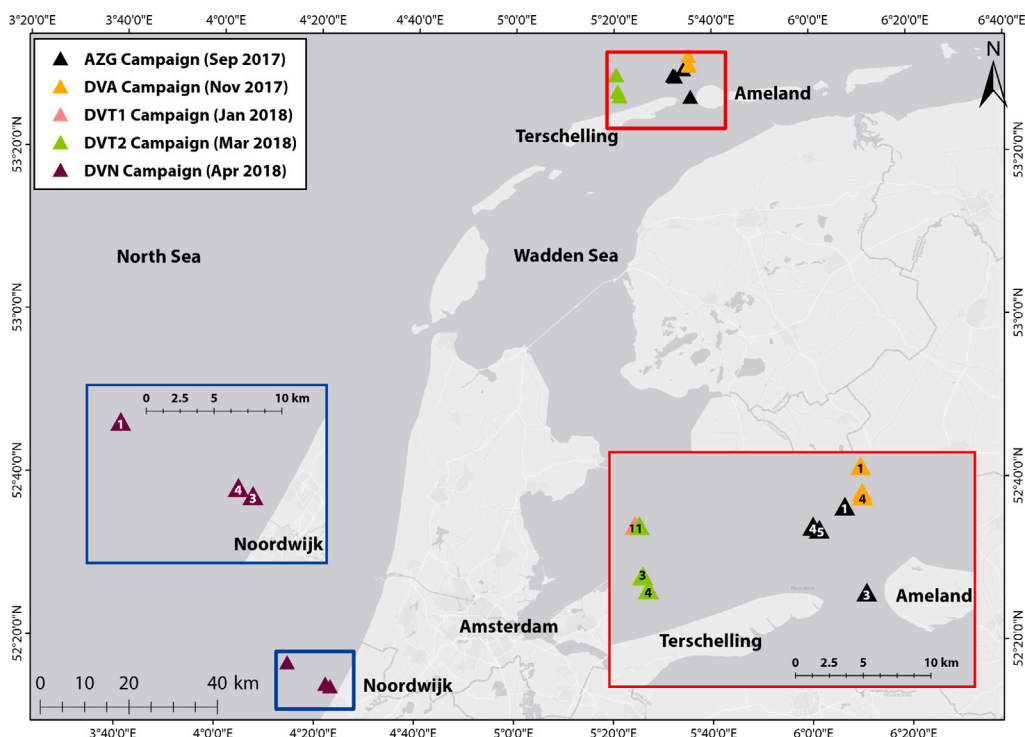
Fig. 1. Overview of the five frame measurement campaigns carried out in the Kustgenese 2.0 project at the four study sites: Ameland Inlet (AZG), and the lower shorefaces of Ameland (DVA), Terschelling (DVT) and Noordwijk (DVN). Note that DVA frame 3 is located very close to DVA frame 4 and is hidden behind it. Frames for DVT campaigns 1 and 2 were placed in approximately the same positions, so their marker symbols overlap. The AZG data are not used in this paper.

This lack of understanding of lower shoreface sediment transport is reflected in results from modeling studies (e.g. Van Rijn, 1997; Aagaard, 2014; Grasmeijer et al., 2022). For example, Van Rijn (1997) found that cross-shore sand transport rates along the Holland Coast, The Netherlands at 20 m water depth were highly uncertain with error bounds up to 100%.

An important reason for the knowledge gap and the absence of good lower shoreface sediment transport models is the limited availability of reliable field data of near-bed sand transport processes. The few valuable existing data sets for the Dutch lower shoreface (e.g. van de Meene and van Rijn, 2000a; Kleinhans and Grasmeijer, 2006) are limited in spatial and temporal coverage and/or do not cover all of the relevant near-bed processes.

Therefore, the Dutch Government Rijkswaterstaat started the *Kust-Genese2.0* (KG2.0) research program in collaboration with research institute Deltares. Part of this program was an extensive field campaign in close collaboration with the Universities of Delft, Utrecht and Twente, via the SEAWAD project. Hydrodynamics, turbidity, sediment composition, bedforms and benthic species distribution were measured at various locations along the Dutch coast (see van Prooijen et al., 2020).

In this paper we will use a subset of the KG2.0 data. We will focus on the near-bed orbital velocities and small-scale bedforms measured simultaneously at three different depths, and at three different Dutch lower shoreface sites, during four campaigns. These data add to existing studies on small-scale wave–current ripples in idealized laboratory settings (e.g. Tanaka and Dang, 1996; Lacy et al., 2007) and in more shallow waters (e.g. Soulsby et al., 2012; Wengrove et al., 2018).

The aims of this paper are: (i) to present these new data and (ii) to evaluate the skill of practical formulas to predict near-bed orbital velocities and small-scale ripple dimensions, which aids to improve our understanding of the physical processes underlying mixed-energy lower shoreface sand transport.

This paper is organized as follows. The fields sites are introduced in Section 2. This section also presents the measurements and explains the data-processing, data-analysis and applied predictive formulas. The measured and predicted near-bed orbital velocities and ripple dimensions are shown in Section 3. The results are discussed in Section 4, followed by the conclusions in Section 5.

2. Methods

2.1. Field sites

The field sites were located on the lower shoreface at the Ameland Inlet, the Terschelling barrier island and at the closed Holland Coast, near Noordwijk (Fig. 1). These sites have different characteristics. The Ameland lower shoreface (DVA) is situated directly offshore the northern part of the ebb tidal delta of Ameland Inlet. It links to the Ameland Inlet field site (AZG) to the south (more information on the AZG campaign can be found in van Prooijen et al. (2020) and Brakenhoff et al. (2020a)). The Terschelling study area is located directly offshore the central part of the island of Terschelling. The shoreface of the barrier islands of the Wadden coast is comparatively unknown. The Noordwijk study area represents the north–south trending closed Holland coast. This area has been studied in the past (see e.g. van de Meene and van Rijn, 2000a,b; Passchier and Kleinhans, 2005; Kleinhans and Grasmeijer, 2006), allowing for intercomparison.

The tide in the North Sea has a predominant semi-diurnal character, with a dominant contribution by the semi-diurnal lunar (M2) component. The mean tidal range is approximately 1.7 m at Noordwijk and 2.0 m at Terschelling and Ameland. At the Dutch lower shoreface the dominant tidal currents have a coast-parallel orientation with average peak depth-averaged velocities of 0.5–0.8 m/s. Waves predominantly come from the south-west, in line with the dominant wind direction. The mean significant wave height is about 1.1 m at Noordwijk, and somewhat higher near Terschelling and Ameland (1.2 m). The highest waves have a north-western orientation. Storms with a return period of 1-year generate waves with a height of about 5.5 m and a period of
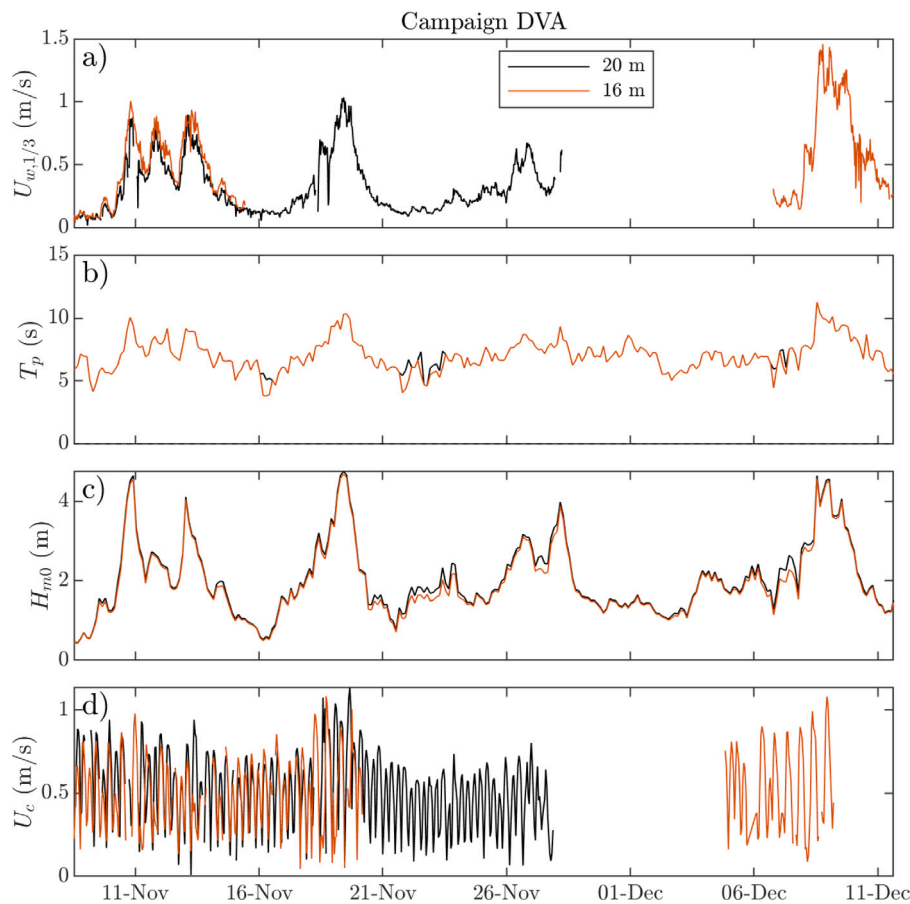
Fig. 2. Time-series of (a) orbital velocity amplitude, (b) peak wave period, (c) significant wave height and (d) depth-averaged current velocity magnitude during the Ameland lower shoreface campaign (DVA), November 2017.

10.5 s near Terschelling and Ameland and 4.8 m and 9.2 s near Noordwijk. More information of the Dutch lower shoreface hydrodynamics and sand transport can be found in Grasmeijer et al. (2022).

The bed sediment at Terschelling and Ameland is similar. It mainly consists of fine sands; the median grain-size is 0.20–0.25 mm (see Table 1). The bed sediments at Noordwijk are coarser with a median grain-size of 0.33 mm.

The interested reader is referred to the paper of van der Spek et al. (2022) for a more detailed description of these field sites.

2.2. Measurements

Custom-made measurement frames were equipped with acoustic Doppler velocimeters (ADVs), an upward-looking acoustic Doppler current profiler (ADCP), a 3D SONAR, and other instruments not used in this paper. The ADV and ADCP instruments incorporated pressure sensors. The frames were deployed on a transect approximately perpendicular to the coast at three different water depths (Table 1). The deployment period varied between 2 and 6 weeks.

Two ADVs, mounted at approx. 0.35 m and 0.65 m above the bed, measured the near-bed velocities with a sampling frequency of 16 Hz during 29-min bursts at an interval of 30 min. The (upward-looking) ADCP measured the velocity profile from 2.3 m above the bed with a frequency of 1.25 Hz with bursts of 30 min at intervals of 30 or 60 min. The cell size was 0.5 m for the shallow deployments (water depths of 10 and 12 m) and 0.8 m for the deeper deployments. The 3D SONAR was mounted approximately 1 m above the bed. It measured the detailed bed morphology with intervals of 1 hr by rotating around its own axis and scanning 200 swaths of the bed.

The ADV on Frame 3 (16 m depth) did not produce reliable data during the first storm event, whereas the ADV on Frame 1 (20 m depth) did not function properly during the second event (DVA campaign). There were no storms and significant wave heights remained below 4 m at Terschelling during the first campaign (DVT1). Therefore, a second Terschelling campaign was carried out (DVT2).

More information on the measurements can be found in van Prooijen et al. (2020).

2.3. Data-processing and data-analysis

The starting point of our study was the processed velocity, pressure and SONAR data (van Prooijen et al., 2020).

The ADV and ADCP pressure sensor data were used to calculate water depth h, assuming a hydrostatic pressure distribution. Given the large depths, near-bed pressures were too small to reliably convert to wave parameters. Alternatively, H_{m0} and spectral peak wave period T_p were extracted from the wave transformation matrix, as described in Grasmeijer et al. (2022). These wave data were used to compute the orbital velocity amplitude, u_w, using linear wave theory. The wave orbital excursion amplitude followed from $a_w = u_w T_p/(2\pi)$.

The data from the ADV located highest above the bed were used to determine orbital velocities in the following way. First, the data were de-trended so that the mean in each burst equals zero. A high pass Fourier filter was applied to filter out velocities with a frequency smaller than 0.05 Hz (period longer than 20 s), focusing on relatively short waves. The resulting orbital velocity vectors were transformed into time series of total orbital velocity in the direction of wave advance, using eigenfunction analysis (see Ruessink et al., 2012). This orbital velocity signal was smoothed using a moving average window
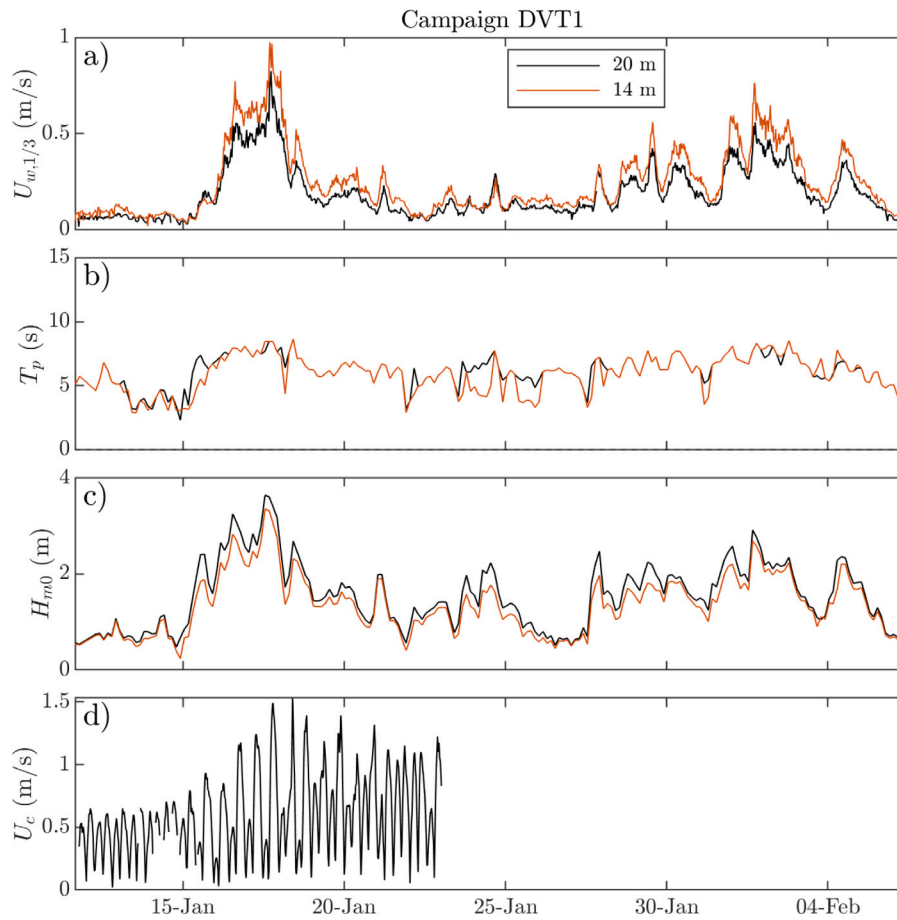
Fig. 3. Time-series of (a) orbital velocity amplitude, (b) peak wave period, (c) significant wave height and (d) depth-averaged current velocity magnitude during the first Terschelling lower shoreface campaign (DVT1), January 2018.

Table 1

Overview of the measurement periods and positions of the frames, median bed grain-size in the surroundings of the frames based on box-core data, as well as the available instrument data. The campaigns are referred to as DVA (*Diepe Vooroever* Ameland): lower shoreface Ameland; DVT1 (Diepe Vooroever Terschelling 1): lower shoreface Terschelling 1; DVT2 (Diepe Vooroever Terschelling 2): lower shoreface Terschelling 2; and DVN (Diepe Vooroever Noordwijk): lower shoreface Noordwijk. The Dutch coordinate system RD (*Rijksdriehoek*) is used.

Campaign	Period	Frame	Location		Approx.	D_{50}	ADV	ADCP	SONAR
			xRD (km)	yRD (km)	depth (m)	(mm)			
DVA	8 Nov - 11 Dec 2017	1	168.339	615.536	20	0.23	X	X	X
		3	168.449	613.779	16	0.20	X	X	X
		4	168.472	613.485	10	0.20		X	X
DVT1	11 Jan - 6 Feb 2018	1	151.671	611.326	20	0.24	X	X	X
		3	152.260	607.627	14		X	X	
DVT2	12 Mar - 26 Mar 2018	1	151.993	611.306	20	0.24	X	X	X
		3	152.249	607.599	14		X	X	
		4	152.662	606.583	10	0.20		X	X
DVN	4 Apr - 15 May 2018	1	76.940	477.601	20	0.33	X	X	X
		3	86.695	472.149	12		X	X	

of 25 samples to filter out turbulence-associated fluctuations. The significant orbital velocity, $u_{w,1/3}$, was defined as the mean of the forward orbital velocity peaks $u_{w,for}$ (or backward orbital velocity peaks, $u_{w,back}$, if these were on average higher) for the highest one-third waves (in terms of the sum of $u_{w,for}$ and $u_{w,back}$).

The wave-related Shields parameter was calculated using:

$$\theta_w = \frac{\tau_w}{(\rho_s - \rho_w) g D_{50}} \tag{1}$$

$$\tau_w = \frac{1}{2} f_w \rho_w u_w^2 \tag{2}$$

where τ_w is the wave-related bed shear stress, $\rho_s = 2650$ kg/m³ the sediment density, $\rho_w = 1025$ kg/m³ the (sea) water density, g the

gravitational acceleration, D_{50} the median grain-size, f_w the wave friction factor and u_w the near-bed orbital velocity amplitude according to linear wave theory. This was preferred over using $u_{w,1/3}$ from the measurements to ensure a continuous orbital velocity time series. The wave friction factor was computed using the formula of Swart (1974) with a roughness height $k_s = 2.5 D_{50}$.

The current-related Shields parameter followed from:

$$\theta_c = \frac{\tau_c}{(\rho_s - \rho_w) g D_{50}} \tag{3}$$

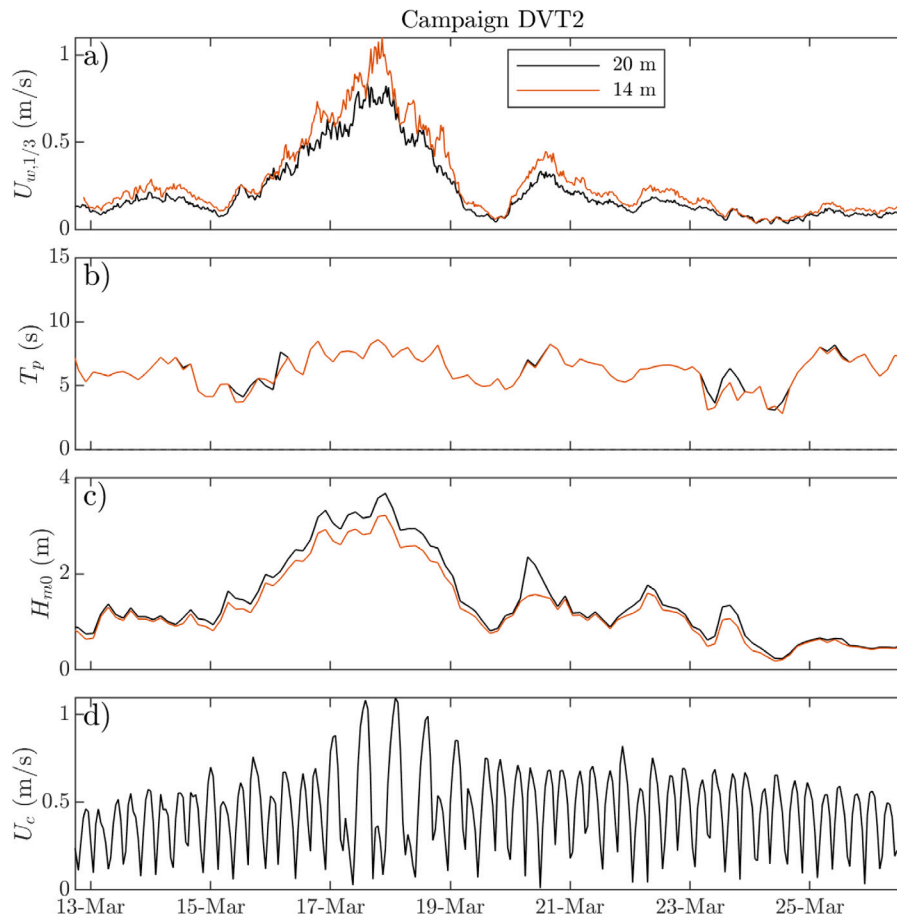$$\tau_c = \frac{1}{2} f_c \rho_w u_c^2 \tag{4}$$

Fig. 4. Time-series of (a) orbital velocity amplitude, (b) peak wave period, (c) significant wave height and (d) depth-averaged current velocity magnitude during the second Terschelling lower shoreface campaign (DVT2), March 2018.

$$f_c = 2\left[\frac{\kappa}{\log_e\left(\frac{30h}{k_s}\right)}\right]^2 \tag{5}$$

where u_c is the depth-averaged velocity, $k_s = 2.5D_{50}$ (the same as the wave-related roughness), and $\kappa = 0.4$ the Von Karmann constant. The depth-averaged velocity was computed based on the data from the two near-bed ADVs, assuming a logarithmic velocity profile Brakenhoff et al. (see 2020a). ADCP data closest to $z = h/e$ were used if no ADV data were available. The depth-averaged velocities were (only) determined for the frames that included a SONAR.

The processing of the SONAR images is described in Brakenhoff et al. (2020a), resulting in bed levels on a regular 2 x 2 m grid with cells of 0.01 x 0.01 m. This includes filtering out perturbations with a length scale smaller than 0.05 m, de-trending to remove the scour hols around the frame legs and a visual image quality assessment. From the remaining images, the ripple height was calculated using $\eta = 2\sqrt{2}\sigma$ with σ the standard deviation of the image. The ripple orientation was found by rotating the images. For each rotation the bedform three-dimensionality (T_b) was calculated using the auto-correlation of the bed elevation data in the x- and y-direction. T_b is a dimensionless parameter, ranging from 0 (indicating a purely two-dimensional bedform) to 1 (indicating a purely three-dimensional bedform). The rotation angle that resulted in the lowest bedform three-dimensionality was taken to be the orientation of the ripples. Using this orientation angle, ripple lengths (λ) were calculated by a wavelet, see Brakenhoff et al. (2020a) for more information. The SONAR could not measure the bed in plane-bed, sheet-flow conditions. These occurred during high energy conditions, when there was a lot of sediment suspension that blocked the acoustic signal.

2.4. Van Rijn (2007) Ripple height predictor

The ripple heights were computed using The Van Rijn (2007) predictor:

$$\eta = \begin{cases} 150D_{50} & \text{for } \psi_{wc} \leq 50 \\ (182.5 - 0.652\psi_{wc})\, D_{50} & \text{for } 50 < \psi_{wc} \leq 250 \\ 20D_{50} & \text{for } \psi_{wc} > 250 \end{cases} \tag{6}$$

with

$$\psi_{wc} = \frac{(u_w^2 + u_c^2)}{\Delta g D_{50}} \tag{7}$$

the wave–current mobility number and $\Delta = (\rho_s - \rho_w)/\rho_w$ the relative sediment density.

This ripple predictor is based on the analysis of many lab and field data sets, and is assumed to be valid for sediment with D_{50} in the range of about 0.1–2.0 mm. The Van Rijn 2007 predictor was chosen because it is a generic formula that is commonly used to compute bed roughness in engineering morphological models like Delft3D. Furthermore, it performed best, together with the Soulsby et al. (2012) predictor, in comparison to small-scale wave–current ripple data on the Ameland ebb-tidal delta (see Brakenhoff et al., 2020b). Note that the Van Rijn 2007 predictor does not consider the angle between waves and currents. It also does not include a threshold for ripple generation, and low-relief bed features (small ripples) are predicted in the sheet-flow regime ($\psi_{wc} > 250$).
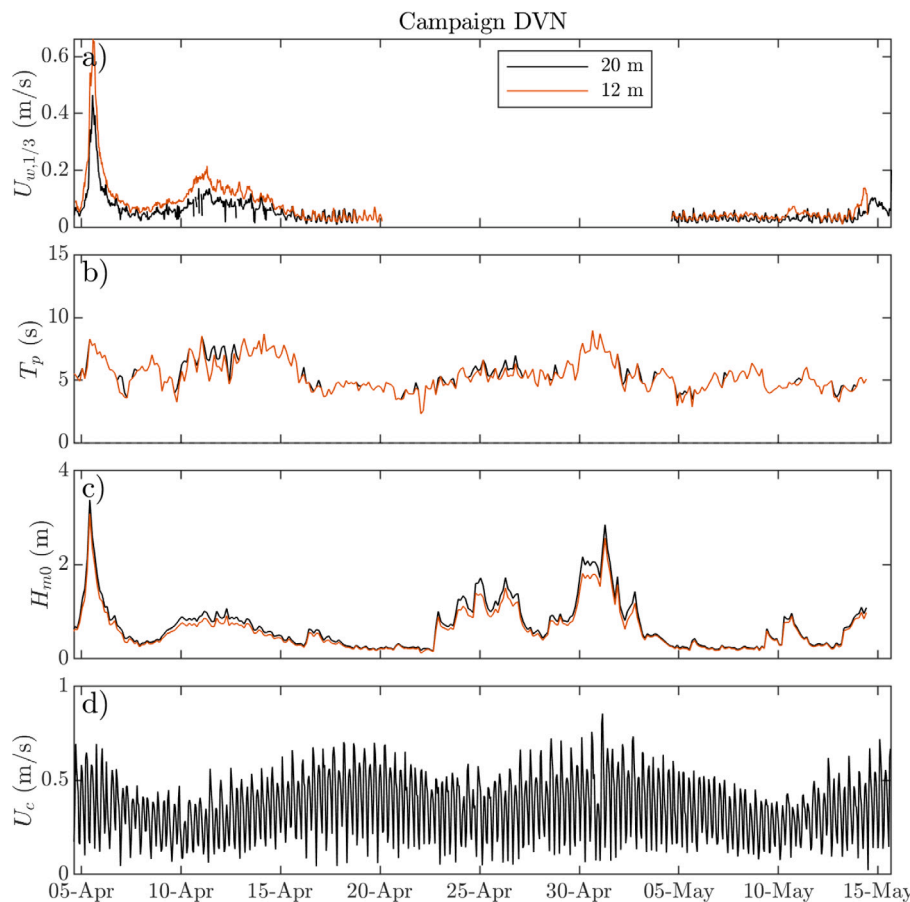
Fig. 5. Time-series of (a) orbital velocity amplitude, (b) peak wave period, (c) significant wave height and (d) depth-averaged current velocity magnitude during the Noordwijk lower shoreface campaign (DVN), April 2018.

3. Results

3.1. Near-bed orbital velocities

Figs. 2–5 show time-series of orbital velocity amplitude, wave period, wave height and depth-averaged current velocity magnitude for all lower shoreface campaigns.

Waves were most energetic during the Ameland campaign (DVA) with wave heights up to about 5 m on 18/19 November and 8/9 December 2017. There were no storms and significant wave heights remained below 4 m at Terschelling during the first campaign (DVT1). During the second campaign (DVT2) the wave height reached a peak value of approx. 5 m on 17 March 2018. The least energetic conditions occurred during the Noordwijk campaign (DVN); the largest wave height (3.4 m) occurred on 5 April 2018. The relative wave height, H_{m0}/h, did not exceed 0.3, indicating that waves were not breaking (Van Rijn, 2013).

The orbital velocity amplitudes correlate well with the wave heights from the wave transformation matrix (see Fig. 6). During low waves ($H_{m0} \leq 0.5$ m) the near-bed orbital velocities were low too ($u_{w,1/3} \leq 0.2$ m/s). During energetic wave conditions ($H_{m0} > 3$ m), the near-bed orbital velocities reached a value of about 1 m/s at the deepest frame and 1.5 m/s at the shallow frame (DVA). Fig. 6 shows that the near-bed orbital velocities can be reasonably well described using linear wave theory.

3.2. Small-scale bedforms

Fig. 7 shows the wave- and current-related Shields values that occurred during the SONAR measurements. This figure shows that the SONAR data cover a large range of conditions: both wave-dominated

($\theta_w > \theta_c$) and current-dominated, and from below initiation of motion ($\sqrt{\theta_w^2 + \theta_c^2} < 0.05$) to the plane-bed/sheet-flow regime ($\sqrt{\theta_w^2 + \theta_c^2} \geq 1.0$). We are aware that this addition of the wave- and current-related Shields values ignores the role of the wave–current angle. The solid lines in Fig. 7 are thus not fully correct, but provide a simple and useful indication of the bed mobility.

The conditions were somewhat more wave- than current-dominated during the Ameland campaign (DVA). The Terschelling (DVT1, DVT2) data points are spread relatively evenly throughout the θ_c-θ_w parameter space. Shields numbers were lowest during the Noordwijk campaign (DVN) as wave heights were relatively low.

The three-dimensionality of the bedforms (T_b) was always very high: values range between 0.96 and 1.00, with an average of 0.99. Visually, ripples appeared to be relatively linear sometimes, see Figs. 8a,c,e as examples at the Noordwijk lower shoreface, frame 1. The T_b values are still 0.97–0.98, because of large deviations both parallel and perpendicular to the ripple crests. The ripples in Fig. 8b,d,f appear more three-dimensional, which is reflected in larger T_b values (0.99).

Fig. 9 and 10 show 2D histograms of ripple heights and lengths, classified according to field site and water depth. The black lines denote the steepness of so-called orbital ripples $\eta/\lambda = 0.17$ (see e.g. Wiberg and Harris, 1994). Orbital ripple dimensions scale with the orbital diameter and generally occur at low mobility numbers (see also O'Donoghue et al., 2006). The average height and length are given by the black dots. The ripple heights vary between 0.01 and 0.03 m, and ripple lengths between 0.08 and 0.20 m. On average, the ripples are 1.6 cm high and 13 cm long. Most ripples have a steepness smaller than 0.17. Ripples were shortest at DVA (11 cm, see Fig. 9). The ripple length is largest at 20 m water depth (0.13 m, see Fig. 10). There is little variation in the (average) ripple height.
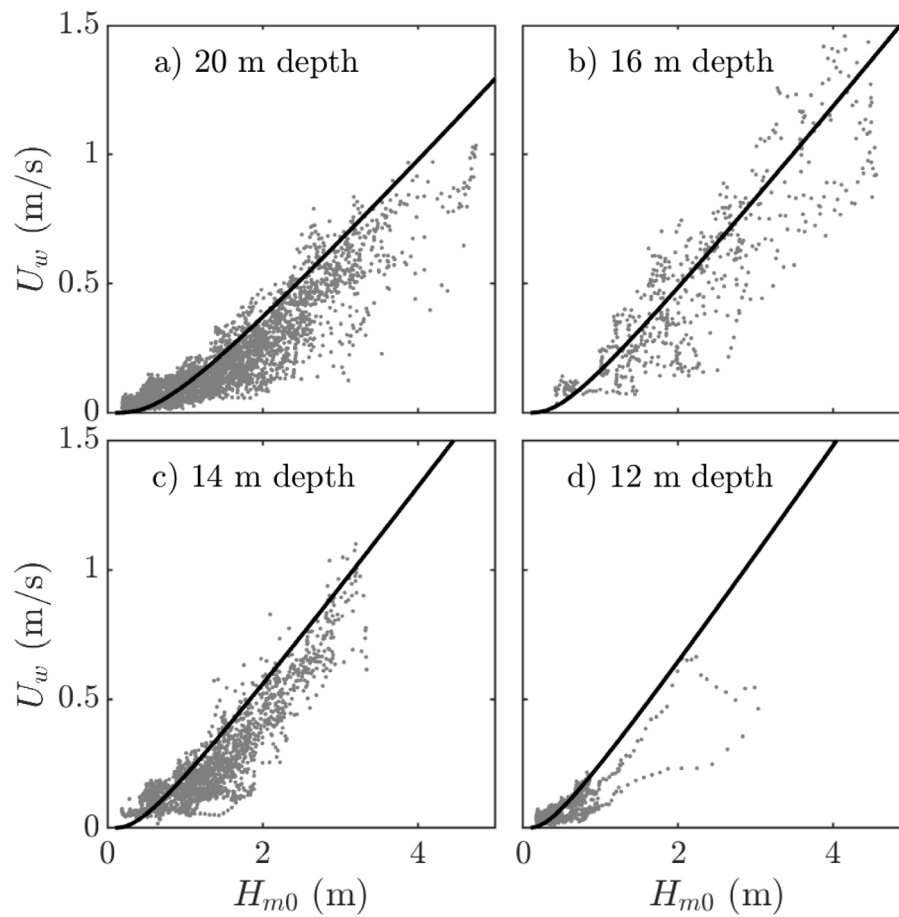
Fig. 6. Relation between orbital velocity amplitude and significant wave height for different water depths: (a) 20 m (DVA, DVT1, DVT2, DVN), (b) 16 m (DVA), (c) 14 m (DVT1, DVT2) and (d) 12 m (DVN). Solid lines: computed using linear wave theory with $T_p = 6H_{m0}^{0.33}$, according to Van Rijn (2013).
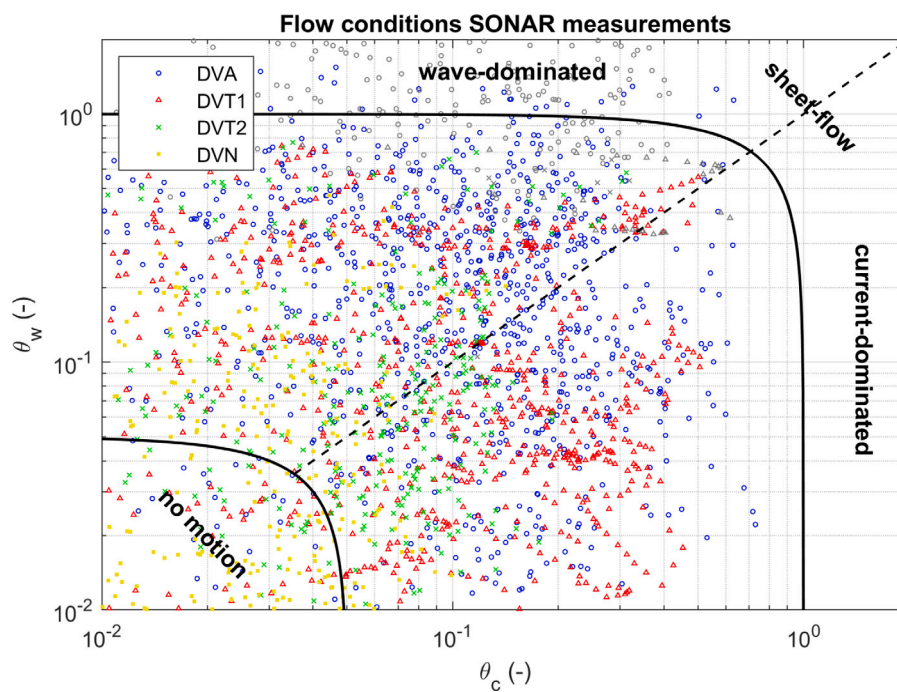

Fig. 7. Wave- and current-related bed shear stress for all SONAR data. The black lines indicate the inception of motion and the transition between the ripple and flat-bed/sheet-flow regime. The dashed lines delineate wave- and current-dominated regions, according to Kleinhans (2005). Gray data points indicate moments with no sonar data.
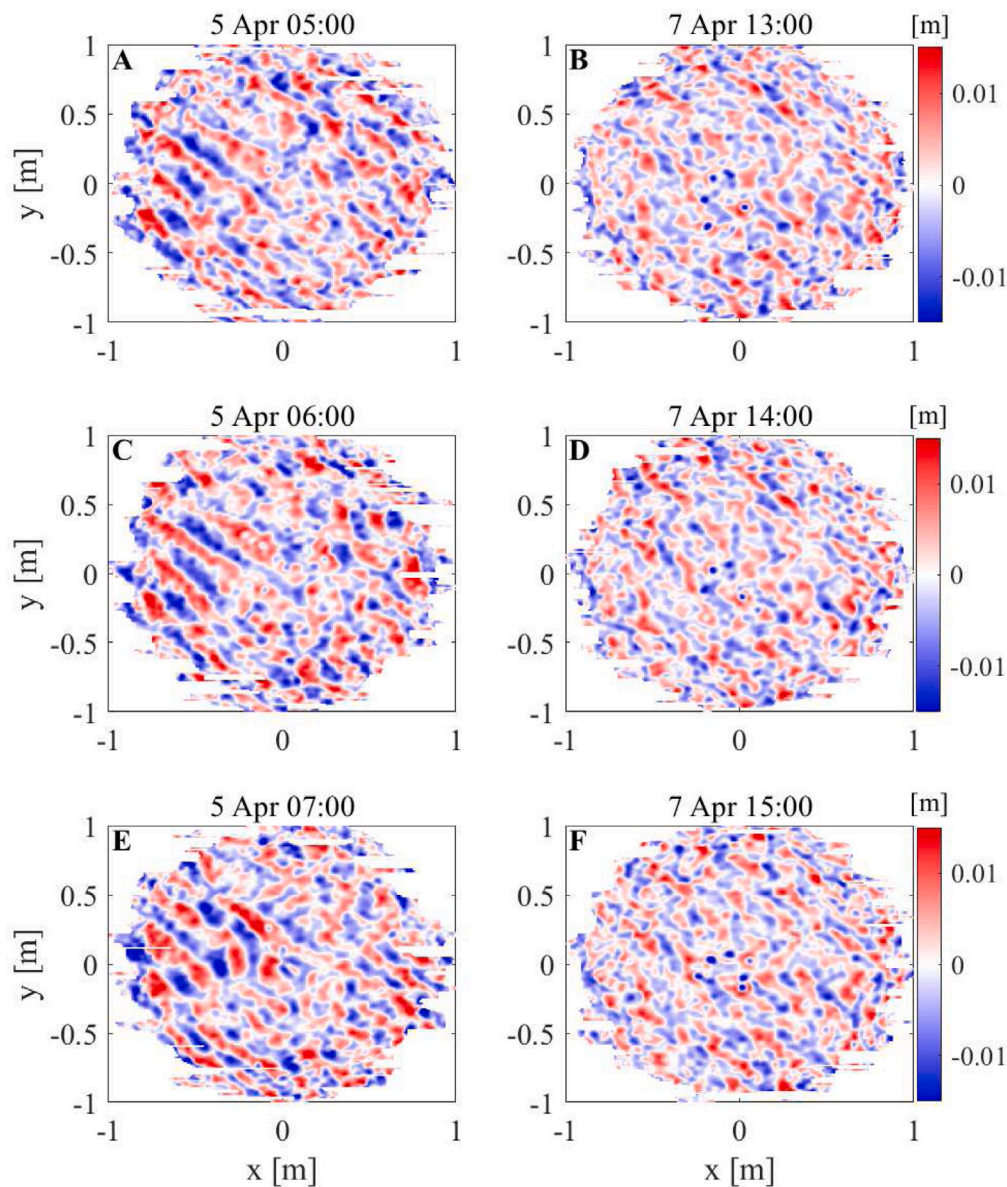
Fig. 8. Examples of ripples at DVN Frame 1.

Fig. 11 shows the hydrodynamics and ripple dimensions at Frame 1 (20 m water depth), Terschelling from 12–23 January 2018 (DVT1 campaign). Wave heights were low at first, but these increased between 16 and 18 January, to become over 3 m high. This results in an increase in the (computed) orbital velocity and wave-related Shields parameter. In this same period, the ripple heights and lengths decreased. Besides this period with higher waves, the ripples have relatively constant dimensions. There is little correlation with the depth-averaged velocity and current-related Shields parameter, which both vary with the tide. This especially applies for the ripple height.

Fig. 12 confirms the correlation between the wave forcing and the ripple dimensions, which were made dimensionless using the orbital excursion amplitude a_w. The measured ripple heights and lengths decrease with the wave-related mobility parameter in line with earlier studies (e.g. Nielsen, 1981; O'Donoghue et al., 2006). There is no correlation between ripple dimensions and the current-related mobility number. For a large number of observations the wave-related mobility parameter was very small ($\psi_w < 1$). These are either relict ripples formed earlier in time when sediment mobility was higher, or these ripples are (partly) generated by the near-bed current.

Most earlier studies such as Nielsen (1981), Wiberg and Harris (1994) and O'Donoghue et al. (2006), largely based on wave-alone data from laboratory experiments, found orbital ripples at low wave mobility. The orbital ripple dimensions scale with the orbital excursion amplitude, $\eta/a_w \approx 0.15 - 0.3$ and $\lambda/a_w \approx 1.2 - 2.2$ depending on wave irregularity and ripple three-dimensionality. Although the dimensionless ripple heights and lengths reach these values at low wave mobility, there is no clear orbital ripple regime with constant η/a_w- and λ/a_w-values.

Fig. 13 and 14 compare the ripple predictor of Van Rijn (2007) with the measured ripple heights. There is a clear relation between the performance of the Van Rijn-predictor and the current strength. For weak currents (low current-related Shields-parameter, θ_c), the ripple heights are overpredicted up to a factor of 4, whereas the heights are underpredicted up to a factor of 4 for strong currents (high θ_c). There is no such clear bias coupled to the wave-related Shields parameter. The overprediction for Shields values below threshold of motion is because the Van Rijn predictor does not include a threshold (Eq. (6)).

The range in predicted ripple heights is much larger than in the observed heights (Fig. 14). According to the Van Rijn-formula the
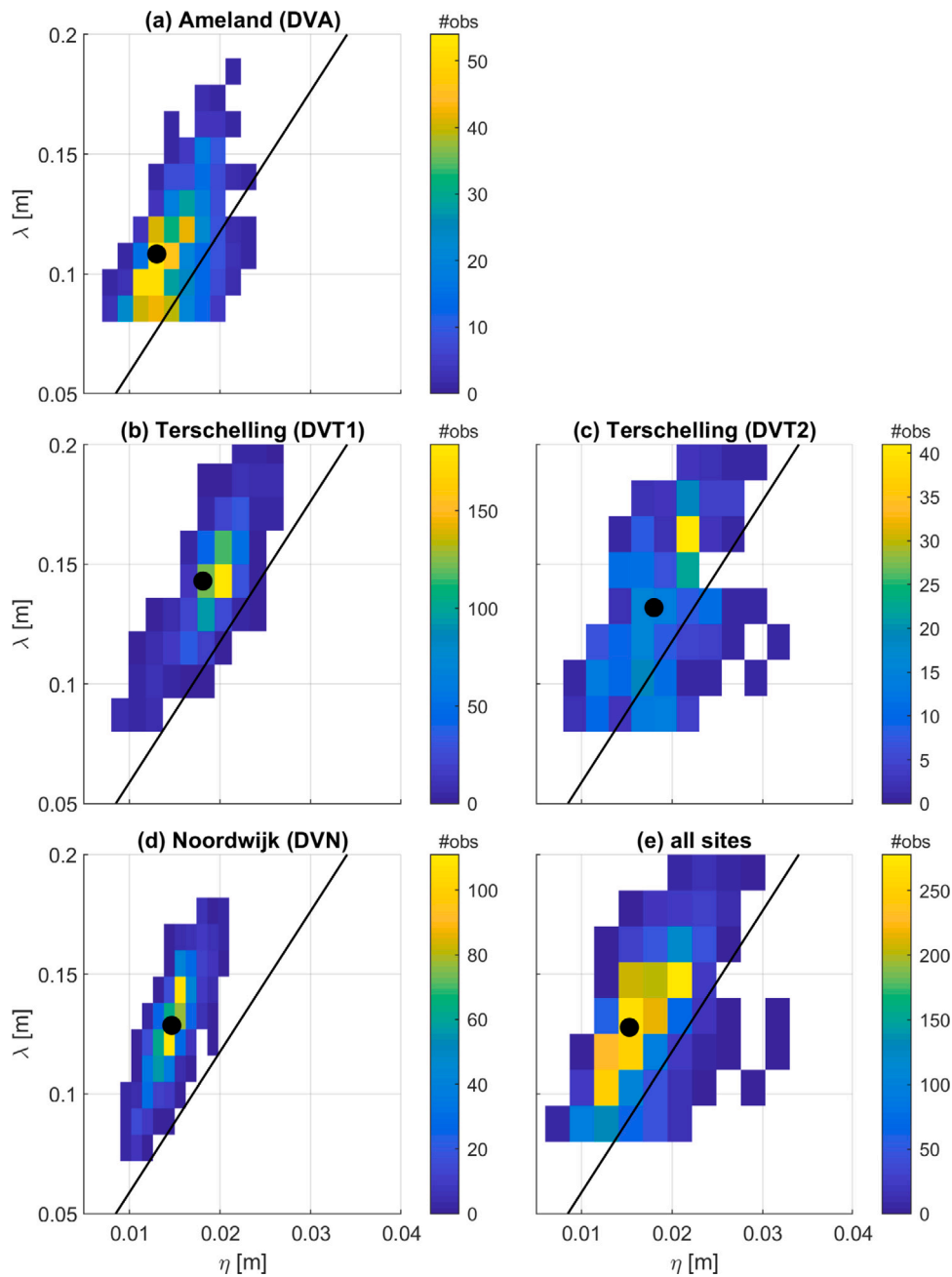
Fig. 9. Histograms of ripple heights and lengths per field site: (a) Ameland (DVA), (b) Terschelling (DVT1), (c) Terschelling (DVT2) and (d) Noordwijk (DVN), and (e) for all data combined. The black line is the equilibrium steepness $\eta/\lambda = 0.17$. The average height and length are given by the black dot.

ripple heights increase (decrease) with a decrease (increase) in current strength which varies within the tidal cycle, whereas the measured ripple heights are mainly controlled by the wave action (see Figs. 11 and 12). This explains the general overprediction for weak currents and the underprediction for strong currents (Fig. 13). The Van Rijn-predictor does capture the general and more slow decrease and increase of ripple heights with the waxing and waning of higher wave events. The Van Rijn-formula generally overpredicts the ripple heights (site-averaged $bias = +1.3$ cm, $RMSE = 1.7$ cm), especially at Noordwijk ($bias = +3.4$ cm, $RMSE = 3.4$ cm).

4. Discussion

The measured near-bed orbital velocities were generally well reproduced by linear wave theory. The input wave conditions were obtained from a wave transformation matrix, or wave look-up table, that enables a swift transformation of measured offshore wave time series to an arbitrary nearshore location. The transformation is based on SWAN wave model calculations. The wave transformation tool was validated using local wave measurements by Grasmeijer (2018). This wave transformation tool was preferred over wave parameters based on near-bed pressure measurements, as the (dynamic) pressure signal was too weak. Yet, it is advised to use in-situ wave measurements, when available, e.g. from a wave buoy.

The measured ripple heights and lengths were fairly constant in time. They do respond to high-wave events, but are nearly independent of the currents that mainly varied with the (M2) tidal. This is remarkable as these currents were strong enough to mobilize sediment and form ripples, as was also predicted by the Van Rijn (2007) formula.
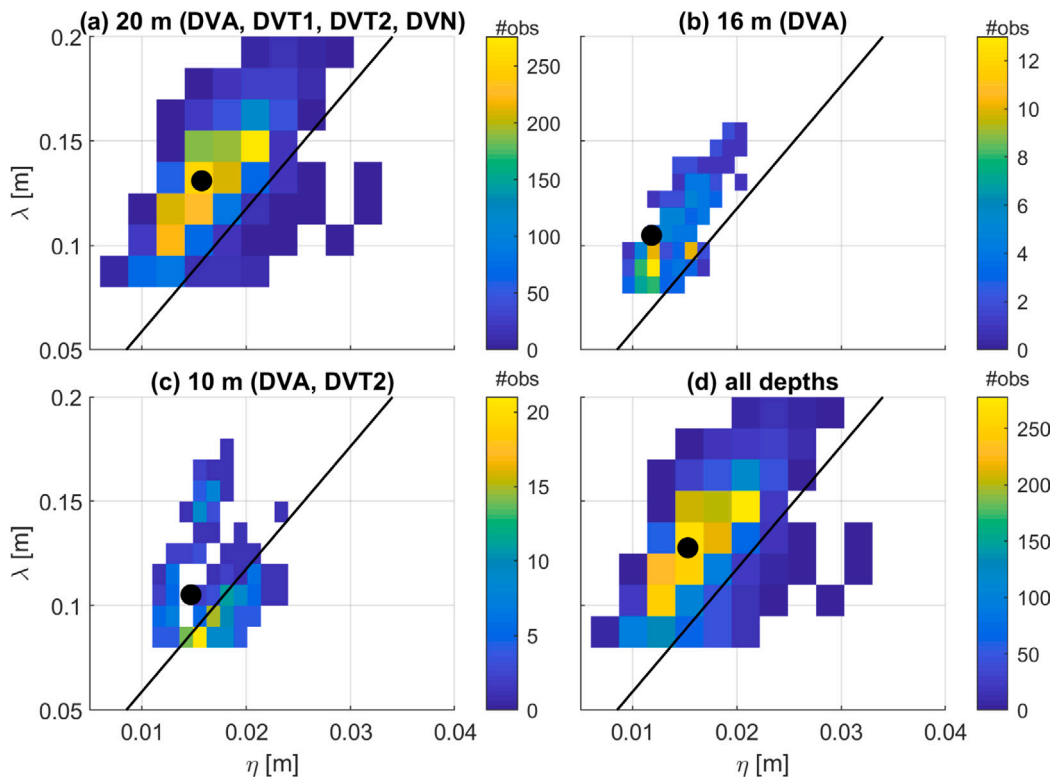
Fig. 10. Histograms of ripple heights and lengths per depth class: (a) 20 m (DVA, DVT1, DVT2, DVN), (b) 16 m (DVA) and (c) 10 m (DVA, DVT2), and (d) for all data combined. The black line is the equilibrium steepness $\eta/\lambda = 0.17$. The average height and length are given by the black dot.
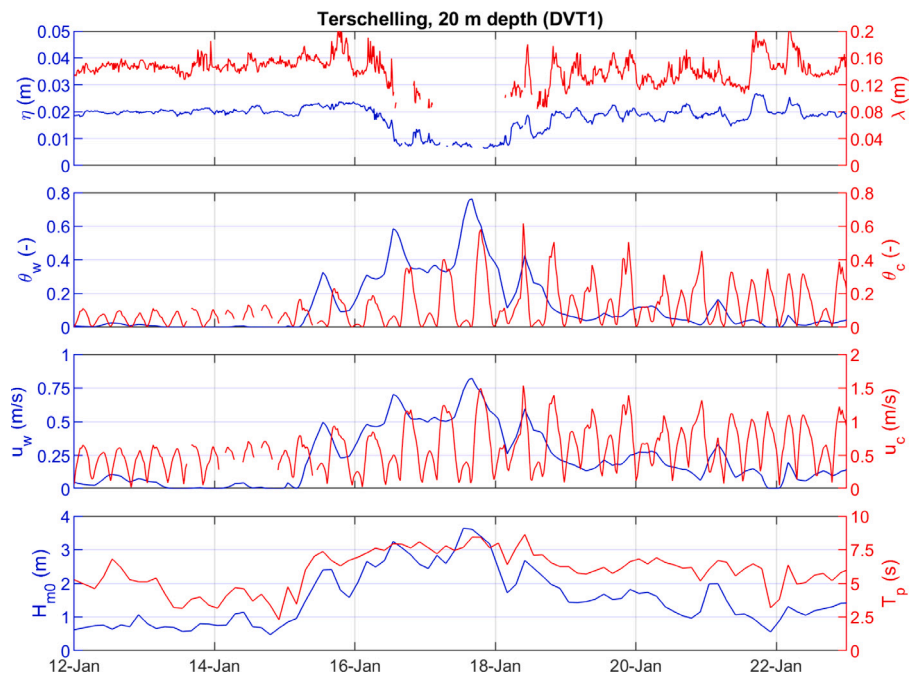

Fig. 11. Time series of (a) ripple dimensions, (b) wave- and current-related Shields parameter, (c) orbital velocity amplitude and depth-averaged current velocity and (d) wave height and period for Frame 1 (20 m water depth) during the DVT1 campaign.

We hypothesize that this is related to the three-dimensionality of the ripples. The dimensions of 3D ripples are mainly controlled by small-scale near-bed hydrodynamics (incl. turbulence), and not so much by large-scale tidal currents (see also O'Donoghue et al., 2006; Brakenhoff et al., 2020a).

Tidal currents are expected to generate bedforms with a larger spatial scale. These so-called mega-ripples are 1–10 m long and tens of cm high (Idier et al., 2004), and thus not measurable by the SONAR with a spatial coverage of 1–2 m. These were measured with multibeam sonar surveys at the lower shoreface of Ameland and Terschelling (van der Spek et al., 2022)
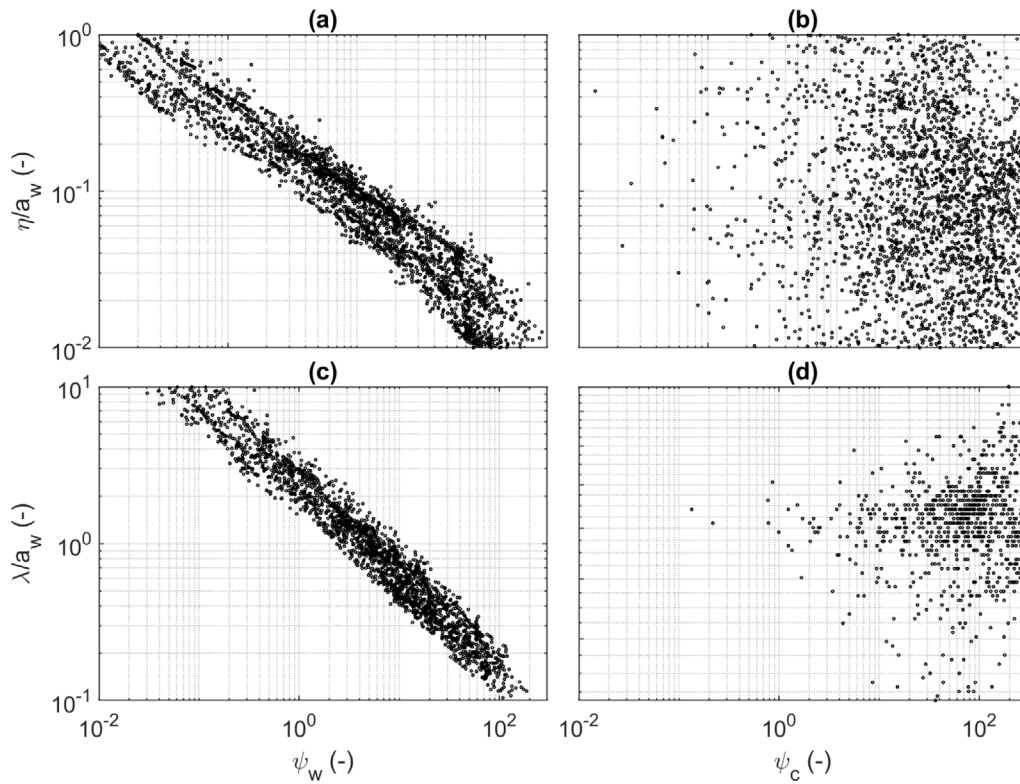
Fig. 12. Non-dimensional ripple height (a,b) and length (c,d) as a function of the wave-related (a,c) and current-related mobility number (b,d).
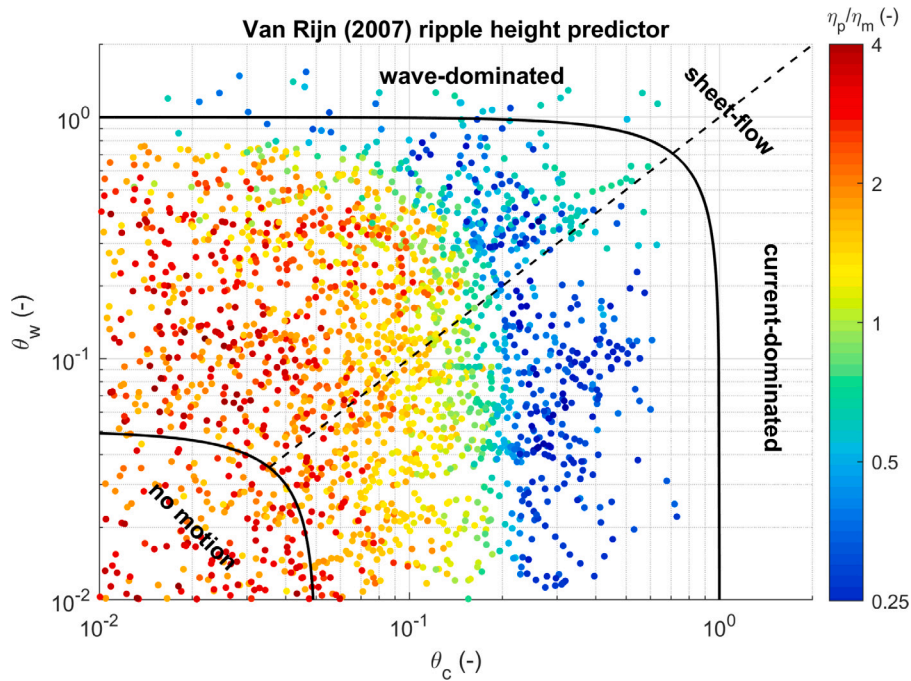

Fig. 13. Ratio of ripple height computed by the Van Rijn (2007) predictor and the measured ripple height (η_p/η_m) as a function of the current- and wave-related Shields parameter. $\eta_p/\eta_m = 1$ denotes perfect agreement. Red colors indicate an overprediction; blue colors an underprediction.

The Ameland lower shoreface (DVA) is situated directly offshore the northern part of the ebb tidal delta of Ameland Inlet. This is different from the Terschelling and Noordwijk sites, which are located offshore from a closed coast. The environmental conditions at DVA are different because of this. However, this is not reflected in the observed ripples that are similar across the three sites. It is hypothesized that the main difference of DVA is the orientation and relative importance of the tidal current, not so much the wave conditions. The ripples mainly respond to the waves, which were not very different, explaining the limited inner-site differences.

The Van Rijn (2007) formula generally overpredicts the measured ripple heights. This was also found by Brakenhoff et al. (2020a), for other ripple predictors as well. These empirical ripple predictors are mainly based on 2D ripple data from wave-dominated laboratory
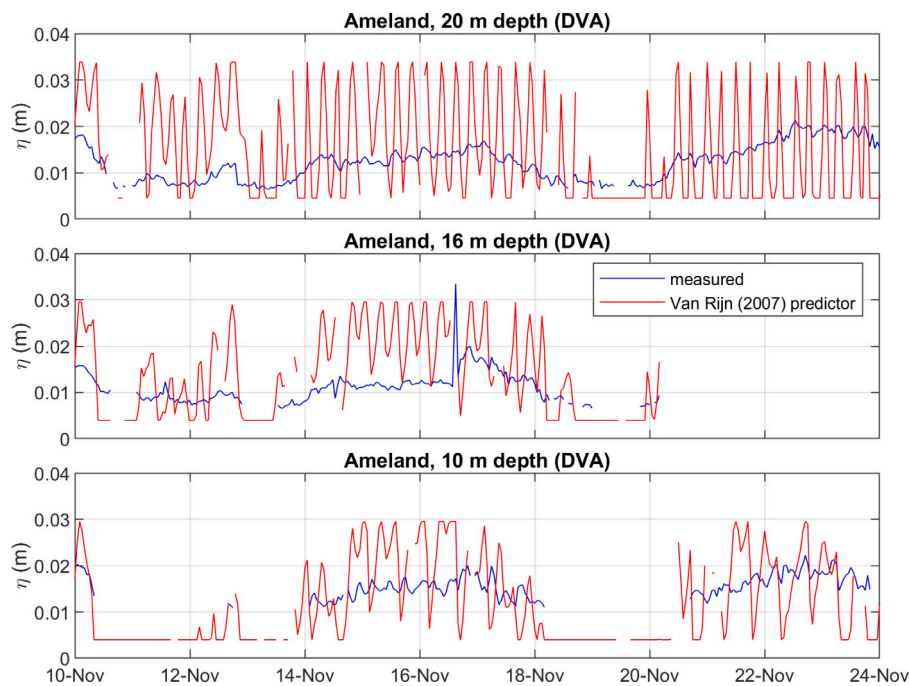
Fig. 14. Time-series of measured and predicted ripple heights at different water depths at the Ameland lower shoreface (DVA).

experiments. Ripple three-dimensionality is known to result in significantly lower ripple dimensions. According to O'Donoghue et al. (2006), equilibrium 3D ripples are 45% lower and 27% shorter than 2D ripples. The sensitivity to the turbulent motions may be the reason why 3D ripples tend to be significantly smaller than 2D ripples. However, at present, there is no full physical explanation for this.

The relatively unknown effect of currents and three-dimensionality on ripple dimensions calls for new controlled full-scale laboratory experiments, including waves and currents, augmented by detailed numerical morphodynamic modeling (such as Marieu et al., 2008) and careful analysis of extensive field data sets. This would build on the work by Lacy et al. (2007) who measured wave–current ripples using an oscillating plate in a flume. They found that ripple height and length decreased with increasing relative current strength. Increasing the relative current strength, or decreasing the wave–current angle, increased the ripple three-dimensionally. These experiments were done with a medium grain-size of 0.27 mm. The questions arises to what degree these observations hold for other sand sizes, and whether orbital flow above a still bed produces the same results as fluid pressure forces are exaggerated on an oscillating bed (Nielsen, 1992).

The wrong prediction of ripple dimensions may have serious implications for engineering morphological models. These models, e.g. Delft3D, include empirical ripple predictors like Van Rijn, to compute bed roughness. Focusing on the more shallow Ameland ebb-tidal delta, Brakenhoff et al. (2020b) found that small-sale ripple-related roughness can make up to 100% of the total roughness. Using measured or predicted ripples resulted in overall differences of 10%–20% in Delft3D-computed current velocity magnitudes and changes of more than 100% in sediment transport. This might also be very well the case for the lower shoreface.

The near-bed orbital velocity and ripple measurements clearly indicate significant sediment mobility at the lower shoreface (depths 10–20 m) under higher wave events ($H_{m0} \gtrsim 2$ m). During regular storms ($H_{m0} \gtrsim 4$ m) orbital velocities reached peak values greater than 1 m/s and ripples became small. Shields numbers indicate that the upper plane-bed, sheet-flow regime with high transport rates confined to a few centimeters thick near-bed layer may be reached during these storms. It is yet unclear what this sediment mobility means for the net

sand transport on the lower shoreface. This will depend on the subtle timing of sediment suspension, wave-mean currents and near-bed orbital velocities. It requires a validated wave–current sand transport model that incorporates 3D effects to compute net sand transport rates on the lower shoreface, and to unravel the controlling sand transport mechanisms.

5. Conclusions

This paper presented new data of near-bed orbital velocities and small-scale bedforms (ripples) at three sites on the Dutch lower shoreface, as measured during four campaigns. The water depths varied between 10 and 20 m. Significant wave heights peaked at 5 m, corresponding to a storm with approx. a 1-year return period. The main novelty of these data lies in the relatively large coverage in space and time, and the simultaneous measurement of near-bed orbital velocities and ripples, which play an important role in lower shoreface sand transport. The data are publicly available at 4TU Centre for Research Data at https://doi.org/10.4121/collection:seawad and https://doi.org/10.4121/collection:kustgenese2.

The near-bed orbital velocity amplitudes were low (≤ 0.2 m/s) during frequently-occurring waves conditions ($H_{m0} \leq 0.5$ m). They reached a maximum value of about 1.5 m/s during a storm event with wave heights up to 5 m. The near-bed orbital velocity amplitudes increase with wave height and decrease with water depth, and are reasonably well described by linear wave theory.

Ripples heights range between $0.01 - 0.03$ m and ripple lengths between $0.08-0.20$ m. The majority of the bedforms were less steep than 0.17, which corresponds to the steepness of orbital ripples at low wave mobility. Ripple lengths decrease with water depth, whereas ripple heights are not strongly correlated to water depth. Ripple dimensions are controlled by wave mobility, with lower and shorter ripples for higher waves. The Van Rijn (2007) formula generally overpredicts the ripple heights, and the variation in time. Unlike predicted, ripple heights do not respond to the tidal currents.

Declaration of competing interest

The authors declare that they have no known competing financial interests or personal relationships that could have appeared to influence the work reported in this paper.

Acknowledgments

This projected was carried out in the context of the *KustGenese* (Coastal Genese) 2.0 project funded by Rijkswaterstaat (RWS). RWS is part of the Dutch Ministry of Infrastructure and Water Management and responsible for the design, construction, management and maintenance of the main infrastructure facilities in the Netherlands. We would like to acknowledge RWS, in particular the vessel crew, for carrying out the lower shoreface measurements. We acknowledge the two anonymous reviewers for their constructive comments that helped to improve the paper.

References

Aagaard, T., 2014. Sediment supply to beaches: Cross-shore sand transport on the lower shoreface. J. Geophys. Res. 119, 913–926. http://dx.doi.org/10.1002/2013JF003041.

Anthony, E.J., Aagaard, T., 2020. The lower shoreface: Morphodynamics and sediment connectivity with the upper shoreface and beach. Earth-Sci. Rev. 210, http://dx.doi.org/10.1016/j.earscirev.2020.103334.

Brakenhoff, L., Kleinhans, M., Ruessink, G., van der Vegt, M., 2020a. Spatio-temporal characteristics of small-scale wave–current ripples on the ameland ebb-tidal delta. Earth Surf. Process. Landf. 45, 1248–1261. http://dx.doi.org/10.1002/esp.4802.

Brakenhoff, L., Schrijvershof, R., van der Werf, J., Grasmeijer, B., Ruessink, G., van der Vegt, M., 2020b. From ripples to large-scale sand transport: The effects of bedform-related roughness on hydrodynamics and sediment transport patterns in delft3d. J. Mar. Sci. Eng. 8, http://dx.doi.org/10.3390/jmse8110892.

Grasmeijer, B.T, 2018. Method for Calculating Sediment Transport on the Dutch Lower Shoreface. Report 1220339-000-ZKS-0041, Deltares, The Netherlands.

Grasmeijer, B., Huisman, B., Luijendijk, A., Schrijvershof, R., van der Spek, A., van der Werf, J., Zijl, F., de Looff, H., de Vries, W., 2022. Modelling of annual sand transports at the Dutch lower shoreface.. Ocean Coast. Manag. 217, http://dx.doi.org/10.1016/j.ocecoaman.2021.105984.

Idier, D., Astruc, D., Hulscher, S.J.M.H., 2004. Influence of bed roughness on dune and megaripple generation. Geophys. Res. Lett. 31, http://dx.doi.org/10.1029/2004GL019969.

Kleinhans, M.G., 2005. Phase diagrams of bed states in steady, unsteady, oscillatory and mixed flows. In: van Rijn, L.C., Soulsby, R., Hoekstra, P., Davies, A.G. (Eds.), Sand Transport and Morphology of Offshore Sand Mining Pits. Aqua Publications, Amsterdam, The Netherlands, pp. Q1–Q16.

Kleinhans, M.G., Grasmeijer, B.T., 2006. Bed load transport on the shoreface by currents and waves. Coast. Eng. 53, 983–996.

Lacy, J.R., Rubin, D.M., Ikeda, H., Mokudai, K., Hanes, D.M., 2007. Bed forms created by simulated waves and currents in a large flume. J. Geophys. Res. Oceans 112, http://dx.doi.org/10.1029/2006JC003942.

Longuet-Higgins, M.S., 1953. Mass transport in water wavesphilos. Trans. R. Soc. 345, 535–581.

Marieu, V., Bonneton, P., Foster, D.L., Ardhuin, F., 2008. Modeling of vortex ripple morphodynamics. J. Geophys. Res. 113, http://dx.doi.org/10.1029/2007JC004659.

Nielsen, P., 1981. Dynamics and geometry of wave-generated ripples. J. Geophys. Res. 86, 6467–6472.

Nielsen, P., 1992. Coastal Bottom Boundary Layers and Sediment Transport. World Scientific, Singapore.

O'Donoghue, T., Doucette, J.S., van der Werf, J.J, Ribberink, J.S., 2006. The dimensions of sand ripples in full-scale oscillatory flows. Coast. Eng. 53, 997–1012.

Passchier, S., Kleinhans, M.G., 2005. Observations of sand waves, megaripples, and hummocks in the dutch coastal area and their relation to currents and combined flow conditions. J. Geophys. Res.- Earth Surf. 110, 1–25. http://dx.doi.org/10.1029/2004JF000215.

Ruessink, B.G., Ramaekers, G., Van Rijn, L.C., 2012. On the parameterization of the free-stream non-linear wave orbital motion in nearshore morphodynamic models. Coast. Eng. 65, 56–63.

Soulsby, R.L., Whitehouse, R.J.S., Marten, K.V., 2012. Prediction of time-evolving sand ripples in shelf seas. Cont. Shelf Res. 38, 47–62. http://dx.doi.org/10.1016/j.csr.2012.02.016.

Swart, D.H., 1974. Offshore Sediment Transport and Equilibrium Beach Profiles (Ph.D. thesis). Delft University of Technology, The Netherlands.

Tanaka, H., Dang, V.T., 1996. Geometry of sand ripples due to combined wave–current flows. 122.

van de Meene, J.W.K, van Rijn, L.C, 2000a. The shoreface-connected ridges along the central Dutch coast. Part 1: field observations. Cont. Shelf Res. 20, 2295–2323.

van de Meene, J.W.K, van Rijn, L.C, 2000b. The shoreface-connected ridges along the central dutch coast. Part 2: morphological modelling. Cont. Shelf Res. 20, 2325–2345.

van der Spek, A., van der Werf, J., Oost, A., Schrijvershof, R., Vermaas, T., 2022. The lower shoreface of the Dutch coast – An overview. Ocean Coast. Manag. (in this issue).

van Prooijen, B.C., Tissier, M.F.S., de Wit, F.P., Pearson, S.G., Brakenhoff, L.B., van Maarseveen, M.C.G., van der Vegt, M., Mol, J.W., Kok, F., Holzhauer, H., van der Werf, J.J., Vermaas, T., Gawehn, M., Grasmeijer, B., Elias, E.P.L., Tonnon, P.K., Santinelli, G., Antolınez, J.A.A., de Vet, P.L.M., Reniers, A.J.H.M., Wang, Z.B., den Heijer, C., van Gelder-Maas, C., Wilmink, R.J.A., Schipper, C.A., de Looff, H., 2020. Measurements of hydrodynamics, sediment, morphology and benthos on ameland ebb-tidal delta and lower shoreface. Earth Syst. Sci. Data 12, 2775–2786. http://dx.doi.org/10.5194/essd-12-2775-2020.

Van Rijn, L.C, 1997. Sediment transport and budget on the central coastal zone of Holland. Coast. Eng. 32, 61–90.

Van Rijn, L.C, 2007. Unified view of sediment transport by currents and waves, I: Initiation of motion, bed roughness, and bed-load. Transp. J. Hydraul. Eng. 133, 649–667.

Van Rijn, L.C, 2013. Principles of Fluid Flow and Surface Waves in Rivers, Estuaries, Seas and Oceans. Aqua Publications, Amsterdam, The Netherlands.

Wengrove, M.E., Foster, D.L., Lippmann, T.C., de Schipper, M.A., Calantoni, J., 2018. Observations of time-dependent bedform transformation in combined wave–current flows. J. Geophys. Res. Oceans 123, 7581–7598. http://dx.doi.org/10.1029/2018JC014357.

Wiberg, P.L., Harris, C.K., 1994. Ripple geometry in wave-dominated environments. J. Geophys. Res. 99, 775–789.